

# Bioinspired One-step Synthesis of Pomegranate-like Silica@Gold Nanoparticles with Surface-Enhanced Raman Scattering Activity

Shujun Zhou,<sup>\*,†</sup> Makoto Maeda,<sup>‡</sup> Eishi Tanabe,<sup>//</sup> Masaru Kubo,<sup>†</sup> and Manabu Shimada<sup>†</sup>

<sup>†</sup> Department of Chemical Engineering, Hiroshima University, 1-4-1 Kagamiyama, Higashi-Hiroshima 739-8527, Japan

<sup>‡</sup> Natural Science Center for Basic Research and Development, Hiroshima University, 1-3-1 Kagamiyama, Higashi-Hiroshima 739-8526, Japan

<sup>//</sup> Western Region Industrial Research Center, Hiroshima Prefectural Technology Research Institute, 3-13-26 Kagamiyama, Higashi-Hiroshima 739-0046, Japan

**KEYWORDS.** Gold-silica; bioinspired synthesis; pomegranate-like nanoparticles; surface-enhanced Raman scattering.

**ABSTRACT:** Gold-silica (Au-SiO<sub>2</sub>) nanohybrids are of great technological importance, and it is crucial to develop facile synthetic protocols to prepare Au-SiO<sub>2</sub> nanohybrids with novel structures. Here we report the bioinspired synthesis of pomegranate-like SiO<sub>2</sub>@Au nanoparticles (P-SiO<sub>2</sub>@Au NPs) via one-step aqueous synthesis from chloroauric acid and tetraethyl orthosilicate mediated by a basic amino acid, arginine. Effects of chloroauric acid, tetraethyl orthosilicate, and arginine on the morphology and optical property of the products are investigated in detail. The P-SiO<sub>2</sub>@Au NPs achieve tunable plasmon resonance depending on the amount of chloroauric acid, which affects the size and shape of the P-SiO<sub>2</sub>@Au NPs. Finite-difference time-domain simulations are performed, revealing that the plasmon peak red-shifts with increasing particle size. Arginine serves as the reducing and capping agents for Au as well as the catalyst for SiO<sub>2</sub> formation, and also promotes the combination of Au and SiO<sub>2</sub>. Formation process of the P-SiO<sub>2</sub>@Au NPs is clarified through time-course analysis. The P-SiO<sub>2</sub>@Au NPs show good sensitivity for both colloidal and paper-based surface-enhanced Raman scattering measurements. They achieve enhancement factor of  $4.3 \times 10^7$ – $8.5 \times 10^7$  and a mass detection limit of *ca.* 1 ng using thiophenol as the model analyte.

## INTRODUCTION

Gold (Au) and its related hybrid materials<sup>1–3</sup> are of technological importance in catalysis,<sup>4</sup> advanced optics,<sup>5</sup> chemical sensing,<sup>6</sup> bio-medicine,<sup>7</sup> solar-energy harvesting,<sup>8</sup> etc.<sup>9</sup> Au-silica (SiO<sub>2</sub>) hybrids are a prominent class of functional materials.<sup>10–12</sup> SiO<sub>2</sub> brings benefits such as enhanced stability,<sup>1, 12, 13</sup> ease of handling,<sup>14, 15</sup> and modified optical property to Au.<sup>16–18</sup> Compositing with SiO<sub>2</sub> also enables new plasmonic materials with exotic structures and enhanced functions.<sup>19–28</sup> For example, Rodríguez-Fernández *et al* used SiO<sub>2</sub> semi-shells as the hard mask on Au nanoparticles (NPs) to obtain Au-SiO<sub>2</sub> Janus nanostars, and derived Au Janus nanostars that were difficult to synthesize with conventional methods.<sup>24</sup> Farrokhtakin *et al* used colloidal SiO<sub>2</sub> as the template to grow radial Au nanowire forests, which displayed strong plasmon coupling compared with isolated Au nanowires.<sup>25</sup> Chomette *et al* used Platonic solids of SiO<sub>2</sub> as the template to fabricate Au-SiO<sub>2</sub> tetrapods, hexapods, and dodecapods with well-controlled composition, morphology and high yield.<sup>26</sup> Self-assembly approaches were also adopted to prepare SiO<sub>2</sub> core-Au

nanoclusters with extraordinary optical<sup>27</sup> and sensing<sup>28</sup> properties. To date, there are very few synthetic protocols for making complex Au-SiO<sub>2</sub> hybrid materials in a facile one-step manner. Most reported methods start with pre-formed Au or SiO<sub>2</sub> NPs for the templated growth or colloidal assembly processes. In addition, the poor vitreophilicity of Au renders it difficult to directly deposit or grow Au on SiO<sub>2</sub> surfaces,<sup>29, 30</sup> and *vice versa*. Procedures such as chemical modification of the SiO<sub>2</sub> surfaces or ligand exchange of the Au surfaces are often required to circumvent the issue.

Amino acids are biomolecules omnipresent in nature. They are known to interact with noble metals,<sup>31, 32</sup> and play an active role in mediating noble metal synthesis as reductant<sup>33</sup> and structure-directing agent.<sup>34</sup> Noble metal NPs such as nanospheres,<sup>33</sup> nanorods,<sup>35</sup> nanocuboids,<sup>36</sup> tetrapods,<sup>37</sup> and chiral nano-objects<sup>38</sup> have been prepared through amino acid-mediated synthesis. On the other hand, amino acids participate in the natural biosilicification processes.<sup>39</sup> The basic amino acids, *i.e.* lysine, arginine, and histidine, were found to mediate SiO<sub>2</sub> precipitation

under mild conditions.<sup>39</sup> Later, bioinspired methods were developed for synthesizing highly monodispersed SiO<sub>2</sub> NPs from tetraethyl orthosilicate using lysine and arginine as the base catalysts.<sup>40-42</sup>

Here we exploit the multifold functions of arginine to achieve the facile one-step synthesis of Au-SiO<sub>2</sub> hybrid NPs with a complex structure that have not been reported before. The NP consists of SiO<sub>2</sub> NPs encapsulated by Au, giving a pomegranate-like interior structure. The pomegranate-like SiO<sub>2</sub>@Au NPs (P-SiO<sub>2</sub>@Au NPs) are synthesized from chloroauric acid and tetraethyl orthosilicate in the presence of arginine in aqueous solution. The synthetic protocol is simple thanks to arginine, which simultaneously reduces Au and catalyzes the silane hydrolysis-condensation reactions. Arginine also promotes the combination of Au and SiO<sub>2</sub> probably through inducing electrostatic attractions. The P-SiO<sub>2</sub>@Au NPs display tunable plasmon resonance as a result of varied particle size and shape. They show good surface-enhanced Raman scattering activity with an enhancement factor of  $4.3 \times 10^7$ – $8.5 \times 10^7$  and a mass detection limit of *ca.* 1 ng, as were experimentally determined using thiophenol as the model analyte. This protocol provides insights for bioinspired synthesis of noble metal-related hybrid materials with new structures and good functions.

## EXPERIMENTAL SECTION

**Materials.** L-Arginine, thiophenol, and cyclohexane were purchased from Nacalai Tesque Inc. Hydrogen tetrachloroaurate(III) tetrahydrate (HAuCl<sub>4</sub> · 4H<sub>2</sub>O) was purchased from FUJIFILM Wako Pure Chemical Corporation. Tetraethyl orthosilicate (TEOS), L-lysine, and trisodium citrate dehydrate were purchased from Tokyo Chemical Industry Co., Ltd. All chemicals were used as received without purification. De-ionized water was used as solvent in all experiments.

**Synthesis of pomegranate-like SiO<sub>2</sub>@Au nanoparticles (P-SiO<sub>2</sub>@Au NPs).** All containers and stirrers were cleaned with *aqua regia* prior to the reaction. As the standard synthetic condition, 24.3 μmol of HAuCl<sub>4</sub> was added to L-arginine aqueous solution (8 mM, 35.2 ml), and then TEOS (2.40 mmol) was added. The mixture reacted at 80 °C in an oil bath with magnetic stirring (500 rpm) for 24 hrs. The P-SiO<sub>2</sub>@Au NPs are generally well-formed within 40–90 °C, and the reaction temperature was fixed at 80 °C for the following experiments. Keeping reaction temperature and time the same, the L-arginine concentration was varied within 2.4–24 mM, and the amount of HAuCl<sub>4</sub> and TEOS was varied within 4.9–48.6 μmol and 0.48–3.84 mmol, respectively, to investigate their effects on the products.

Control experiment to examine the role of TEOS was conducted through employing preformed SiO<sub>2</sub> sol in place of TEOS for the synthesis. First, SiO<sub>2</sub> nanoparticles (SNPs)

having a size of *ca.* 15 nm was synthesized as previously reported.<sup>41</sup> Briefly, arginine (0.21 mmol) was dissolved in water (34.5 ml) followed by the addition of TEOS (12.5 mmol). The mixture reacted at 60 °C with magnetic stirring (500 rpm) for 24 hrs. Next, arginine was dissolved in 35.2 ml of water to a concentration of 8 mM, and then 24.3 μmol of HAuCl<sub>4</sub> and the preformed SNP sol (SiO<sub>2</sub> 2 wt%, 3 ml) were added. The mixture reacted at 80 °C in an oil bath with magnetic stirring (500 rpm) for 24 hrs.

Control experiment to examine the role of arginine was conducted by replacing it with lysine for reducing HAuCl<sub>4</sub> in water. Lysine is a basic amino acid capable of reducing Au and often-used for SNP synthesis.<sup>40, 42</sup> It has a different side group from that of arginine. Briefly, lysine was dissolved in 35.2 ml of water to a concentration of 8 mM, followed by the addition of 24.3 μmol of HAuCl<sub>4</sub>. The mixture reacted at 80 °C in an oil bath with magnetic stirring (500 rpm) for 24 hrs.

**Characterization.** A transmission electron microscope (TEM, JEM-2010, JEOL) operating at 200 kV was used for structural observation. A field-emission scanning electron microscope (FE-SEM, S-5200, Hitachi High-Technologies) operating at 3 kV was used to examine the surface morphology. A field-emission transmission electron microscope (FE-TEM, JEM-3000F, JEOL) operating at 297 kV was employed for high-resolution electron microscopy and elemental analysis. It is equipped with the scanning transmission electron microscopy (STEM) detectors with the NORAN System SIX for energy dispersive X-ray spectroscopy (EDS). The reactions gave SNPs as a by-product, and the suspensions were washed once through centrifugation (8000 rpm, 10 min), decanting, and redispersion in water to remove the excess SNPs before electron microscopic observations. Powder X-ray diffraction (XRD) spectrum was measured with the Bruker D2 Phaser spectrometer operating at 30 kV and 10 mA using the Cu Kα radiation ( $\lambda = 1.54$  Å). Sample for XRD measurement was prepared by directly drying the suspension into powder. The hydrodynamic size was measured with dynamic light scattering (DLS) technique using a Zetasizer Nano ZS instrument (Malvern Inc.). Samples for DLS measurements were prepared by washing the as-synthesized suspensions thrice with water through centrifugation and finally re-dispersing the centrifugates with arginine aqueous solution (8 mM). The UV-Vis extinction spectra were measured with the JASCO V-650 spectrometer. The pH value was measured using the CyberScan pH110 meter (EUTECH Instruments).

**Surface-enhanced Raman scattering (SERS) measurements.** SERS performances of the P-SiO<sub>2</sub>@Au NPs were evaluated using thiophenol (TP) as the probe molecule. The P-SiO<sub>2</sub>@Au NPs were synthesized with 8 mM arginine in 35.2 ml water, 2.40 mmol of TEOS and varying amounts of HAuCl<sub>4</sub> (12.1, 24.3, and 36.4 μmol) at 80 °C. The as-synthetic suspensions were sedimented through centrifugation and decantation once, and then diluted

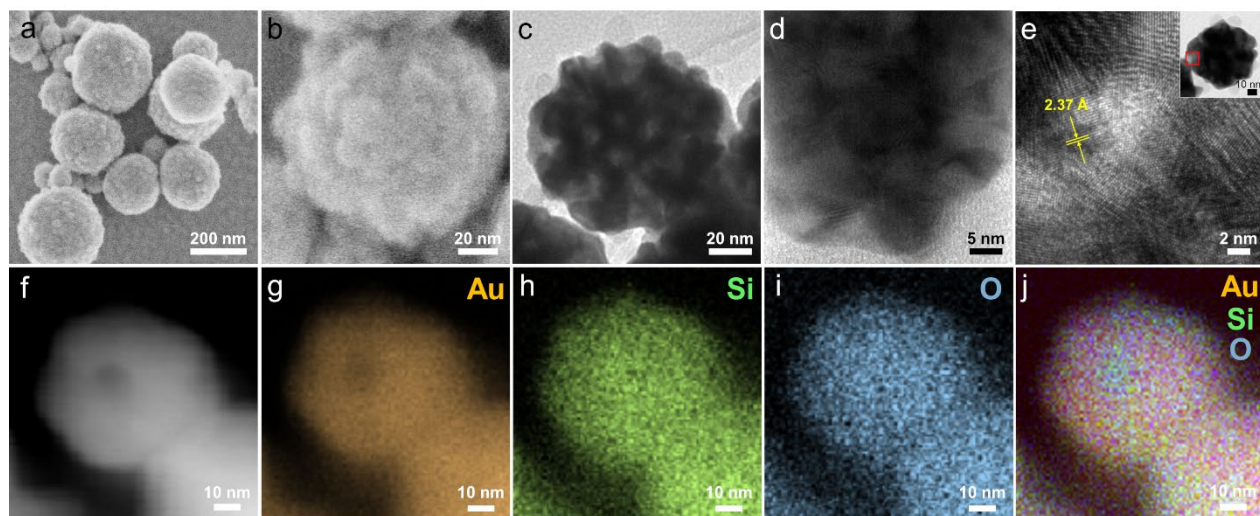


**Figure 1.** (a-b) SEM, (c-e) TEM, and (f) high-angle annular dark-field STEM images of P-SiO<sub>2</sub>@Au NPs prepared with the standard synthetic condition. (g-j) STEM-EDS elemental mappings of the particle shown in (f). Inset in (e) indicates with a red square the imaging area in the corresponding TEM image.

with water to a concentration of 0.25 mM of Au. Proper amount of the TP ethanolic solution was added to the diluted P-SiO<sub>2</sub>@Au NP suspensions to reach TP concentration of  $10^{-5}$  -  $10^{-8}$  M in the aqueous solution. For example, 20  $\mu$ l of  $10^{-3}$  M TP solution was added to 1.98 ml of diluted P-SiO<sub>2</sub>@Au NP suspension to reach a final TP concentration of  $10^{-5}$  M. The mixture was shaken with hand and kept static for 15 minutes for the TP molecules to adsorb to the particle surface. Raman spectra of neat TP was measured for reference. All the liquid samples were measured in a standard quartz cuvette (3.5 ml) using a portable Raman spectrometer (Ocean Optics, QE65000) with a 785 nm diode laser and a fiber optic Raman probe. The laser power was 4 mW and the integration time was 10 s.

The paper-based SERS measurements were conducted as follows. Laboratory filter paper (Advantech, No. 5C) was impregnated in the as-synthesized P-SiO<sub>2</sub>@Au NP suspension for several days. The filter paper turned from white to bluish-purple, indicating the adsorption of P-SiO<sub>2</sub>@Au NPs. The filter paper loaded with P-SiO<sub>2</sub>@Au NPs (P-FP) was dried at 80 °C for 10 minutes, cut into 1 × 1 cm<sup>2</sup> pieces, and ready for use. For comparison, spherical Au NPs were synthesized with the citrate-reduction method.<sup>43</sup> Paper substrates loaded with spherical Au NPs (Au-FP) were prepared through the above-mentioned procedures. TP was deposited by dropping 0.9  $\mu$ l of  $10^{-3}$  M,  $10^{-4}$  M,  $0.5 \times 10^{-4}$  M, and  $10^{-5}$  M TP solution at the center of the P-FP and Au-FP substrates; evaporating the solvent gave dried spots containing 100 ng, 10 ng, 5 ng, and 1 ng of TP, respectively. The portable Raman spectrometer (Ocean Optics, QE65000) with a 785 nm diode laser and a fiber optic Raman probe was used. The laser power was 3 mW and the integration time was 10 s. Raman signals from P-FP (or Au-FP) without TP were set as the background. Three individual measurements were conducted and averaged to give the SERS spectra.

### Finite-difference time-domain (FDTD) simulation.

Numerical simulations of the optical property were performed with a commercial FDTD software (Lumerical FDTD Solutions 8.0). The extinction, scattering, and absorption cross sections and the electromagnetic field distribution were calculated through addressing the three-dimensional Mie scattering problem. Water was set as the dielectric background medium with a refractive index of 1.33. Models of the P-SiO<sub>2</sub>@Au NP were constructed according to TEM observation. The optical constant for Au was obtained from the data by Johnson and Christy,<sup>44</sup> and that for SiO<sub>2</sub> was obtained from the data by Palik.<sup>45</sup> A total-field scattered-field source with a wavelength range of 400-900 nm was applied as the incident radiation. The perfectly matched layer was adopted as the boundary condition.

## RESULTS AND DISCUSSION

**Characterization of P-SiO<sub>2</sub>@Au NPs.** The suspensions were washed to remove the excess SNPs in the background (Figure S1a) before electrostatic imaging. Figure 1 shows the typical electron microscopic images of P-SiO<sub>2</sub>@Au NPs. They have bumpy surfaces as shown by SEM images (Figure 1a, 1b). Bright-field TEM image shows different contrasts from the particle's interior (Figure 1c), indicating a composite structure. High-resolution TEM image shows that the strong-contrast interior component (black) as well as the particle surface are crystalline (Figure 1d). The lattice fringes have an inter-plane distance of ca. 2.37 Å (Figure 1e), corresponding to that of the Au (111) crystal planes. XRD analysis also confirmed the face-centered cubic crystal structure of Au (JCPDS 4-0783) (Figure S1b). Meanwhile, the weak-contrast component (grey) from the interior may be pore or an amorphous material. Elemental analysis was conducted with the STEM. A region without isolated SNPs in the background (Figure 1f) was carefully selected to minimize their interference on the analysis. The EDS mappings

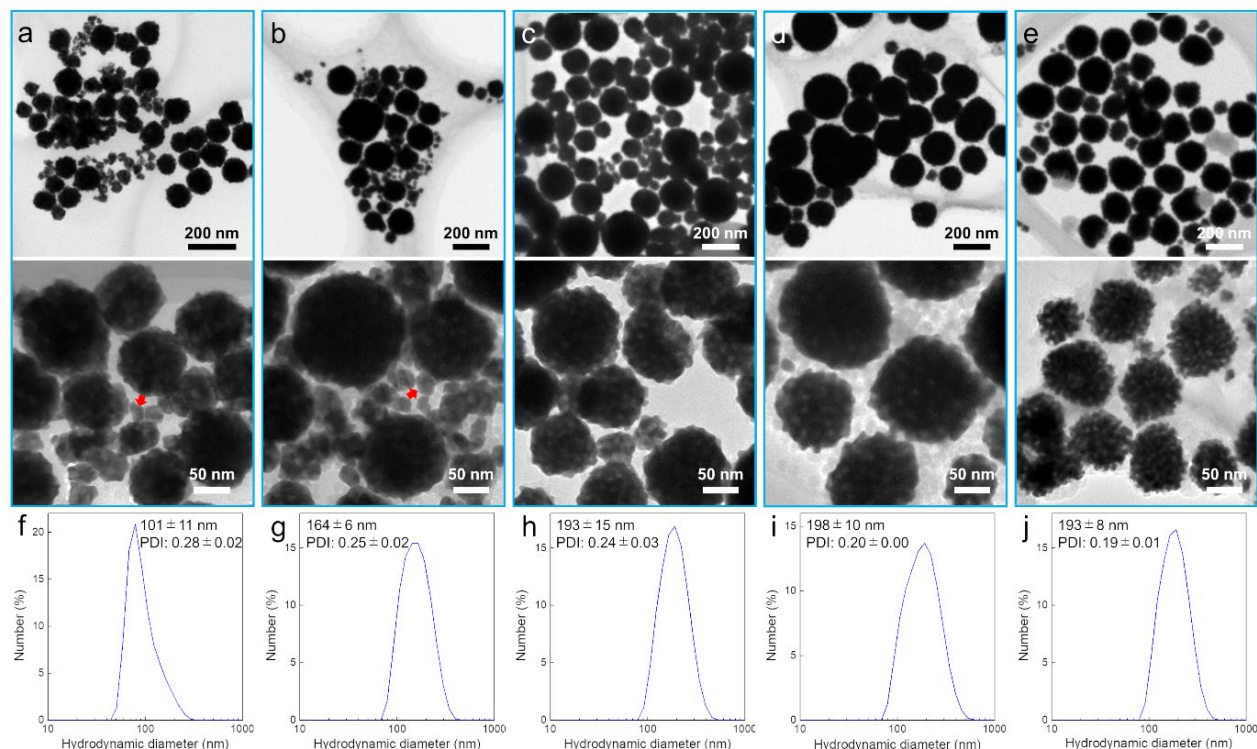


**Figure 2.** TEM images of P-SiO<sub>2</sub>@Au NPs synthesized with (a) 4.9, (b) 12.1, (c) 24.3, (d) 36.4, and (e) 48.6 μmol of HAuCl<sub>4</sub>. Hydrodynamic sizes of P-SiO<sub>2</sub>@Au NPs synthesized with (f) 4.9, (g) 12.1, (h) 24.3, (i) 36.4, and (j) 48.6 μmol of HAuCl<sub>4</sub>.

show the existence of Au, Si, and O in the NP (Figure 1g-1j). The distribution of Au (Figure 1g) fits well with the contours of the NP in the corresponding STEM image (Figure 1f), agreeing with TEM observation that the particle surface is Au (Figure 1d). The existence of Si and O (Figure 1h-1i) indicates that the NP also contains SiO<sub>2</sub>. The synthesis involves reduction of HAuCl<sub>4</sub> and the hydrolysis-condensation of TEOS at the same time. The former reaction yields Au, while the latter gives SiO<sub>2</sub>. The SiO<sub>2</sub> in the form of SNPs leads to the formation of the above structure as will be discussed in *Effect of TEOS* section. SNPs embedded in the Au matrix give the weak-contrast component of the interior structure in TEM image (Figure 1c), hence the structure can be described as a pomegranate-like SiO<sub>2</sub>@Au structure.

**Effects of HAuCl<sub>4</sub>.** Products synthesized with varying amounts of HAuCl<sub>4</sub> are shown in Figure 2. With 4.9 μmol of HAuCl<sub>4</sub>, P-SiO<sub>2</sub>@Au NPs below 100 nm along with irregular Au particles (indicated by arrow) are mainly observed (Figure 2a). Increasing the addition of HAuCl<sub>4</sub> leads to P-SiO<sub>2</sub>@Au NPs of larger sizes (Figure 2b-2d). The irregular Au particles (indicated by arrow) still exist with 12.1 μmol of HAuCl<sub>4</sub> (Figure 2b); while well-formed P-SiO<sub>2</sub>@Au NPs are mainly observed with 24.3 and 36.4 μmol of HAuCl<sub>4</sub> (Figure 2c, 2d). The interior structures of P-SiO<sub>2</sub>@Au NPs synthesized with 4.9-36.4 μmol of HAuCl<sub>4</sub> are similar according to the TEM images. The particles become less spherical with 48.6 μmol of HAuCl<sub>4</sub> (Figure 2e), and the

interior structure appears different from those observed in Figure 2a-2d. The weak-contrast SiO<sub>2</sub> component of the interior structure is sphere-like in Figure 2a-2d, while it appears slender wire-like in Figure 2e. A high dose of HAuCl<sub>4</sub> introduces high ionic strength, which may alter the growth kinetics of Au to affect the shape of the particle.

The hydrodynamic size of P-SiO<sub>2</sub>@Au NPs was analyzed with DLS measurements. It raises from ca. 101 nm to ca. 198 nm with increased addition of HAuCl<sub>4</sub> from 4.9 to 36.4 μmol (Figure 2f-2i). The polydispersity indices (PDI) are within 0.20-0.28, indicating low degree of polydispersity.<sup>46</sup> The PDI decreases with increased addition of HAuCl<sub>4</sub>. This can be understood by referring to the TEM images, which show that the irregular Au particles and relatively small P-SiO<sub>2</sub>@Au NPs disappear with increasing addition of HAuCl<sub>4</sub> (Figure 2a-2c), and finally the P-SiO<sub>2</sub>@Au NPs having sizes around 200 nm dominate (Figure 2d). The P-SiO<sub>2</sub>@Au NPs synthesized with 48.6 μmol of HAuCl<sub>4</sub> have a hydrodynamic size of ca. 193 nm with low degree of polydispersity (Figure 2j), as is consistent with TEM observation.

UV-Vis extinction spectra of the P-SiO<sub>2</sub>@Au NP suspensions (Figure 3a) display plasmon peaks due to the surface plasmon resonance.<sup>47</sup> The plasmon peak red-shifts from ca. 580 nm to ca. 730 nm with increasing peak addition of HAuCl<sub>4</sub> (Figure 3b). The plasmon property is sensitive to particle



size, particle shape, aggregation states, and the surrounding dielectric environments.<sup>47</sup> Because the P-SiO<sub>2</sub>@Au NPs are dispersed in the same aqueous

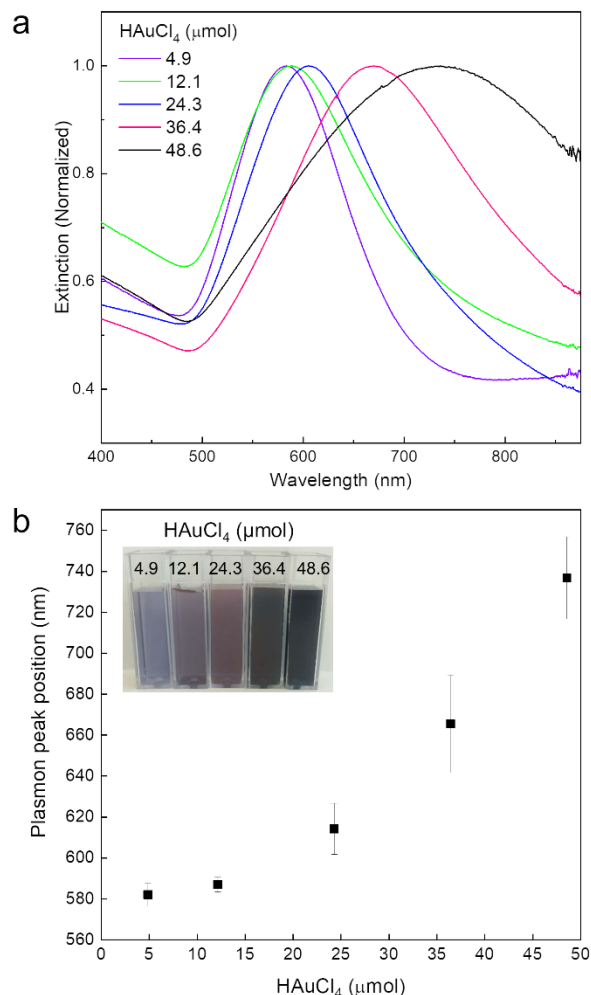


**Figure 3.** (a) Normalized UV-Vis extinction spectra of the suspensions synthesized with varying amounts of HAuCl<sub>4</sub>. (b) Plasmon peak position shifts with the amount of HAuCl<sub>4</sub>; each data point was collected by averaging 3 different samples. Inset is the photo of the suspensions.

environment, the particle size and shape should be important factors affecting their plasmon property. According to TEM and DLS results, the particle size effect can be considered important for P-SiO<sub>2</sub>@Au NPs synthesized with 4.9–36.4 μmol of HAuCl<sub>4</sub>. Regarding the P-SiO<sub>2</sub>@Au NPs synthesized with 48.6 μmol of HAuCl<sub>4</sub>, their plasmon peak red-shifts by *ca.* 60 nm, although their particle size is similar to those synthesized with 36.4 μmol of HAuCl<sub>4</sub>. Because their interior structure has changed at a high dose of HAuCl<sub>4</sub>, the particle shape effect may contribute to the peak shift.

FDTD simulation was performed to probe the effects of particle size on the plasmon property. The size of embedded SNPs and their inter-particle distances are estimated from the TEM images and simplified models of the P-

SiO<sub>2</sub>@Au NPs are built for the simulation (Figure S2). The overall particle size of P-SiO<sub>2</sub>@Au NP is increased through increasing the number of embedded SNPs. Figure 4 shows the calculated

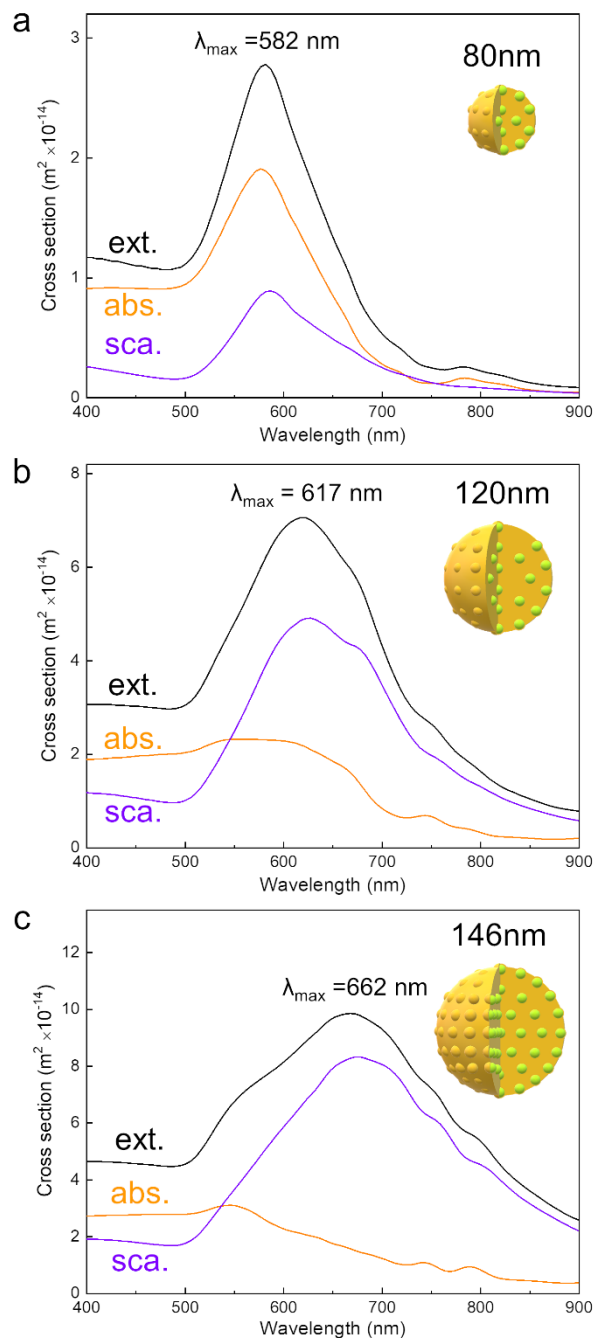


**Figure 4.** Calculated extinction (ext.), scattering (sca.), and absorption (abs.) cross sections of P-SiO<sub>2</sub>@Au NPs with varying sizes: (a) 80 nm, (b) 120 nm, and (c) 146 nm.

results of extinction, scattering, and absorption cross sections of P-SiO<sub>2</sub>@Au NPs with varying sizes. The extinction maxima shifts from 582 nm to 662 nm as the particle size increases from 80 nm to 146 nm. Extinction cross section is the sum of scattering and absorption cross sections. As the particle becomes larger, the scattering component dominates over the absorption component, and red-shifts to cause the red-shift of the extinction maxima. Although the real samples are not perfectly monodisperse and contain P-SiO<sub>2</sub>@Au NPs with moderate size distributions, the simulation result helps to understand how P-SiO<sub>2</sub>@Au NPs of different sizes contribute to the overall plasmon property. It well explains the tendency of red-shifting plasmon peak with increasing addition of HAuCl<sub>4</sub> (4.9-36.4  $\mu$  mol) due to the emergence of large and the disappearance of small P-SiO<sub>2</sub>@Au NPs. Increasing the particle size can also be viewed as increasing the number of SNPs in the P-SiO<sub>2</sub>@Au NPs, suggesting that the SNPs provide a means to tune the plasmon property.

**Effects of TEOS.** The effects of TEOS were investigated through varying the amounts of TEOS under otherwise the same synthetic conditions. In the absence of TEOS, HAuCl<sub>4</sub> is reduced by arginine to Au, which deposits as a blueish-purple coating on the inner wall of the glass vial; in contrast, the liquid phase is colorless and transparent (Figure 5a, inset). TEM observation of the liquid sample finds very few but only dense Au aggregates (Figure 5a). The P-SiO<sub>2</sub>@Au NPs begins to be observed when 0.48 mmol of TEOS is added (Figure 5b), but a considerable portion of Au still deposits on the glass vial and the experimental reproducibility is low. The addition of over 1.20 mmol of TEOS ensures the formation of P-SiO<sub>2</sub>@Au NPs with good yields (Figure 5c); however, too much TEOS results in more SNPs as a by-product (indicated by the arrow in Figure 5d).

The above observations indicate the importance of TEOS for enabling the P-SiO<sub>2</sub>@Au NPs. The reaction mixture is initially a two-phase system when TEOS is added to the aqueous solution containing HAuCl<sub>4</sub>. Stirring can break TEOS into small oil droplets that might serve as template for Au deposition to form the pomegranate-like structure. To test this possibility, TEOS was replaced with an equal volume of cyclohexane while keeping other parameters the same as in the standard synthetic condition. Similar to the reaction without TEOS, Au deposits on the inner wall of the glass vial, leaving the liquid phase colorless and transparent (Figure 5e, inset). TEM observation of the liquid sample finds merely dense Au aggregates (Figure 5e). Therefore it is unlikely that the TEOS oil droplets serve as template for the pomegranate-like structure. In parallel to the Au reduction reaction, TEOS reacts to form SNPs through the hydrolysis-condensation reactions catalyzed by arginine.<sup>41</sup> To examine the role of SNPs in the formation of pomegranate-like structure, TEOS was replaced with preformed SNP sol (ca. 15 nm, Figure S3) for the synthesis. A homogenous dark-purple suspension is obtained and TEM observation confirms the existence of pomegranate-

like structures (Figure 5f). They have concave-like features with a size of ca. 14 nm, agreeing with the size of the preformed SNPs. It is likely that the formation of pomegranate-like structure involves the enclosure of SNPs by Au. Observations in Figure 5a and Figure 5e indicate a tendency of the reduced Au to deposit on SiO<sub>2</sub> surface, *i.e.* the inner wall of glass vial. The preformed SNPs can provide a substrate for Au

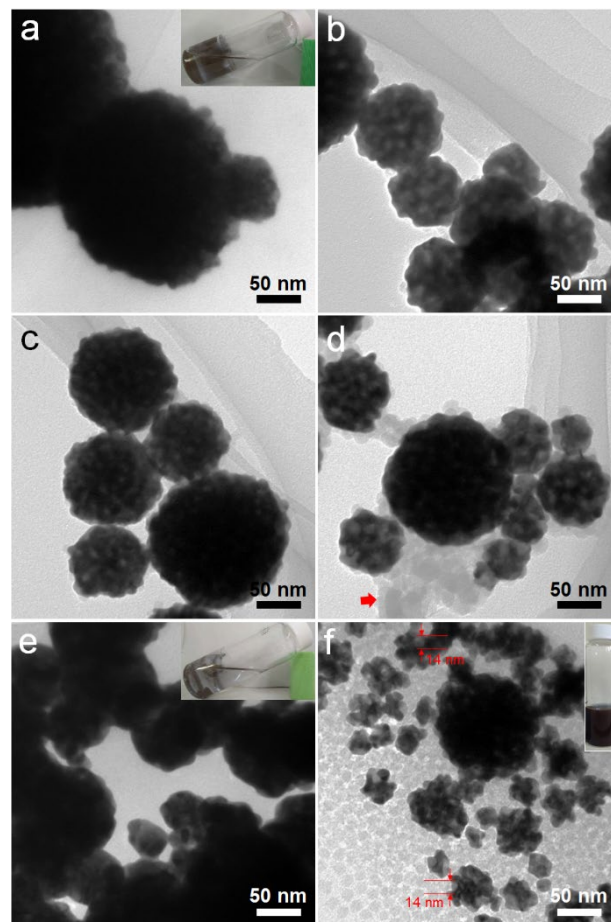


**Figure 5.** TEM images of samples synthesized with (a) 0, (b) 0.48, (c) 1.20, (d) 3.84 mmol of TEOS; (e) cyclohexane in place of TEOS, and (f) preformed SNP sol in place of TEOS. Insets in (a), (e), and (f) show the macroscopic appearance of the sample after reaction.

deposition. Hence TEOS is important as a source to SNPs that enable the formation of P-SiO<sub>2</sub>@Au NPs.

**Effects of arginine.** Arginine serves as the reducing and capping agents for Au and the catalyst for SNP formation at the same time, hence it has vital effects on the structure. Samples synthesized with varying arginine concentration are examined. The optimal arginine concentration for forming P-SiO<sub>2</sub>@Au NPs is found to be 8-16 mM (Figure 6a). Tadpole-like (Figure 6b) and branched (Figure 6c) structures form with less-than-optimal arginine concentration; while fusion of the P-SiO<sub>2</sub>@Au NPs (indicated by

the arrows in Figure 6d) occurs at a high arginine concentration. A sufficient amount of arginine should be required to catalyze the reactions of TEOS to form SNPs<sup>40, 41</sup> indispensable to the pomegranate-like structure. Though the SNPs can possibly form at arginine concentration as low as 0.2 mM,<sup>41</sup> the pomegranate-like structures require at least 8 mM of arginine, indicating that a major portion of arginine contributes to affect Au.

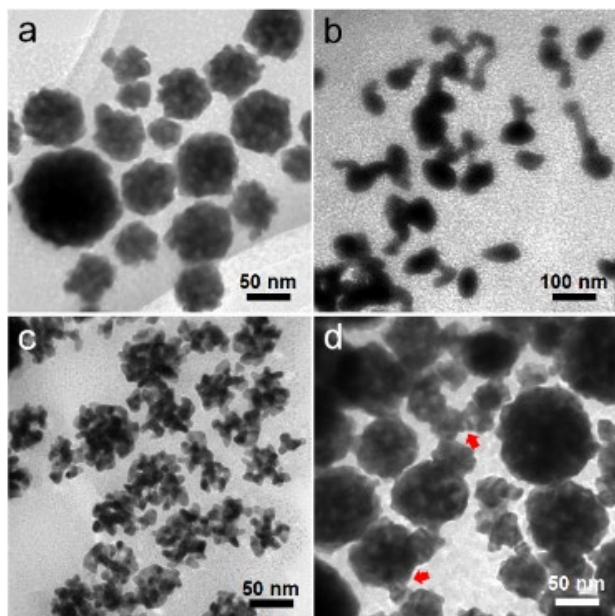


**Figure 6.** TEM images of samples synthesized with arginine concentration of (a) 16, (b) 2.4, (c) 4, and (d) 24 mM under otherwise the same reaction conditions.

Arginine interacts with  $\text{HAuCl}_4$  through forming arginine- $\text{AuCl}_4^-$  complex<sup>48</sup> and reduces it to Au. UV-Vis spectra shows that the peak of  $\text{AuCl}_4^-$  at 305 nm disappears after dissolving arginine (Figure S4), suggesting the formation of arginine- $\text{AuCl}_4^-$  complex.<sup>37</sup> Arginine can adsorb to the Au surface upon reduction and affect the Au- $\text{SiO}_2$  interaction. Previous observation (Figure 5a) indicates that arginine can promote Au deposition on  $\text{SiO}_2$  surface. Its effects were further examined through control experiment using lysine, a basic amino acid with a different side group, to reduce  $\text{HAuCl}_4$  in water. The reaction gives a homogeneous purple suspension with very little Au deposits on the glass vial (Figure S5). The apparent differences suggest that arginine's guanidinium group may be critical in promoting the combination of Au and  $\text{SiO}_2$ . The guanidinium group is characterized by a very high  $\text{pK}_a$  (ca. 13.8).<sup>49</sup> It tends to be protonated and cause the Au surface to be positively charged through surface adsorption.<sup>50</sup> Meanwhile the reaction system has alkaline pH condition (Table S1), under which the  $\text{SiO}_2$  (IEP: pH 2-3) surface is negatively charged with the deprotonated silanol groups.<sup>51</sup> Such reverse surface charge states favor the Au deposition on  $\text{SiO}_2$ . In the presence of SNPs, the reduced Au can enclose them to form the pomegranate-like structure.

**Formation process.** The formation process of the P- $\text{SiO}_2$ @Au NPs is revealed through time-course TEM observation of the products collected at different reaction time (Figure 7). Discrete Au nanocrystals form within 10 min (Figure 7a), and then grow into irregularly shaped particles after 30 min of reaction (Figure 7b). Dendritic structures are observed after 60 min (Figure 7c). Their characteristic morphology suggests that they are possibly formed through diffusion-limited aggregation.<sup>52</sup> The dendritic structures shrink into structures with densified cores and

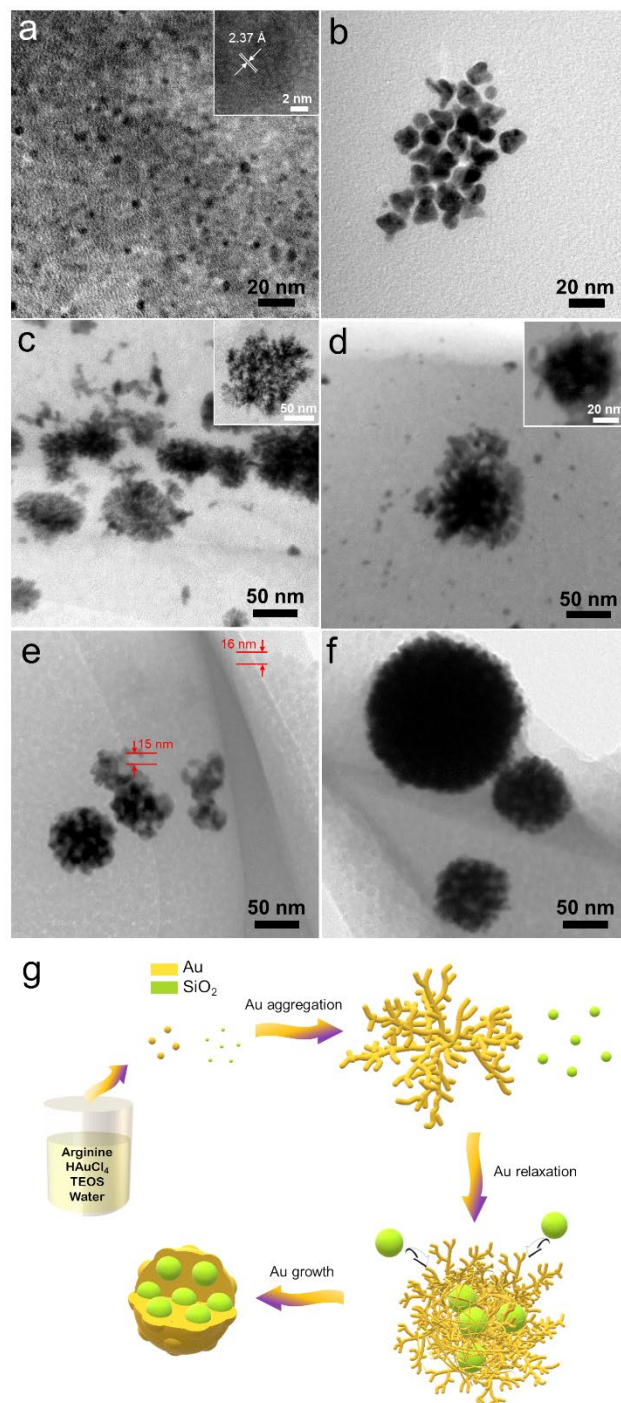




**Figure 7.** TEM images of the products collected at different time during reaction: (a) 10, (b) 30, (c) 60, (d) 90, (e) 120, and (f) 150 min. The standard synthetic condition was adopted. Inset in (a) is the high-resolution TEM image of the corresponding sample. Insets in (c) and (d) show other observed structures in the corresponding samples. (g) Schematic illustration of the formation pathways of P-SiO<sub>2</sub>@Au NPs.

dendritic peripherals after 90 min (Figure 7d). Some particle has pomegranate-like interior in the core region (Figure 7d, inset). Observation of the shrinking dendritic structure is analogous to previous reports.<sup>53-54</sup> It is attributable to the relaxation process for the dendritic structures to grow into more stable forms.<sup>55</sup> After 120 min, the P-SiO<sub>2</sub>@Au NP emerge and intermediate products with concave-like feature can be observed (Figure 7e). Size of the concave-like feature (*ca.* 15 nm) is comparable to that of the SNPs in the background (*ca.* 16 nm), reflecting the SNPs' shaping effects on the Au structure. After 150 min, well-developed P-SiO<sub>2</sub>@Au NPs can be observed (Figure 7f). The color of the suspension changed from colorless, to light blue, and to purple-blue, and remained stable after 240 min of reaction (Figure S6), indicating the completion of Au reduction. A typical reaction time of 24 hrs was adopted for the complete reaction of TEOS. The pH of the suspension during reaction is relatively stable (Table S2) due to the buffering capability of arginine.<sup>56</sup> Figure 7g summarizes the supposed formation pathways of the P-SiO<sub>2</sub>@Au NPs. Arginine initiates two reactions: the reduction of HAuCl<sub>4</sub> to Au and the hydrolysis-condensation reactions of TEOS into SNPs. The Au primary particles aggregate to form dendritic structures, which then relax into more stable forms through shrinking. The shrinking Au dendritic structures enclose the SNPs while continuously grow by adding in new Au atoms from the solution to form the pomegranate-like structure.

**SERS performances.** SERS activity of the P-SiO<sub>2</sub>@Au NPs is evaluated with TP as the model analyte for its ability to chemically adsorb to Au surfaces. The Raman spectrum of the neat TP is measured for reference (Figure 8a). Raman modes typical of the TP molecule are observed at 976, 1001, 1068, 1560 cm<sup>-1</sup>, which can be assigned to the  $\beta_{\text{ring}}$  (ring in-plane bending),  $\beta_{\text{CH}}$  (C-H in-plane bending),  $\beta_{\text{ring}} + \nu_{\text{CS}}$  (ring in-plane bending and C-S stretching), and  $\nu_{\text{CC}}$  (C-C stretching) modes, respectively.<sup>57</sup> Figure 8b shows the SERS spectra of trace amounts of TP in aqueous solution with P-SiO<sub>2</sub>@Au NPs. The SERS peaks have shifted frequencies and different intensity patterns from those of the Raman spectrum (neat TP), because SERS measurements detect TP molecules adsorbed to the Au surface. Surface adsorption can change the molecule's orientation, leading to different vibrational frequencies and relative Raman scattering cross sections in the SERS spectra.<sup>58-60</sup> TP can be detected down to 10<sup>-8</sup> M owing to the enhancement effects by the P-SiO<sub>2</sub>@Au NPs (Figure 8b and Figure S7). The enhancement factor (EF) is calculated using the formula<sup>61</sup>

$$EF = \frac{I_{\text{SERS}}}{N_{\text{SERS}}} \times \frac{N_{\text{Raman}}}{I_{\text{Raman}}}$$

$I_{\text{SERS}}$  and  $I_{\text{Raman}}$  are the integrated peak area of a specific signal in the SERS and Raman spectrum, respectively. Here the signal at 1049 cm<sup>-1</sup> for SERS and that at 1068 cm<sup>-1</sup> for Raman are used for calculation.  $N_{\text{SERS}}$  and  $N_{\text{Raman}}$  are the number of excited TP molecules in the laser excitation volume for SERS and Raman measurements, respectively. Because the SERS and Raman spectra are measured with the same amount of liquid samples in the standard quartz cuvette, their laser excitation volumes are the same.  $N_{\text{SERS}}$  and

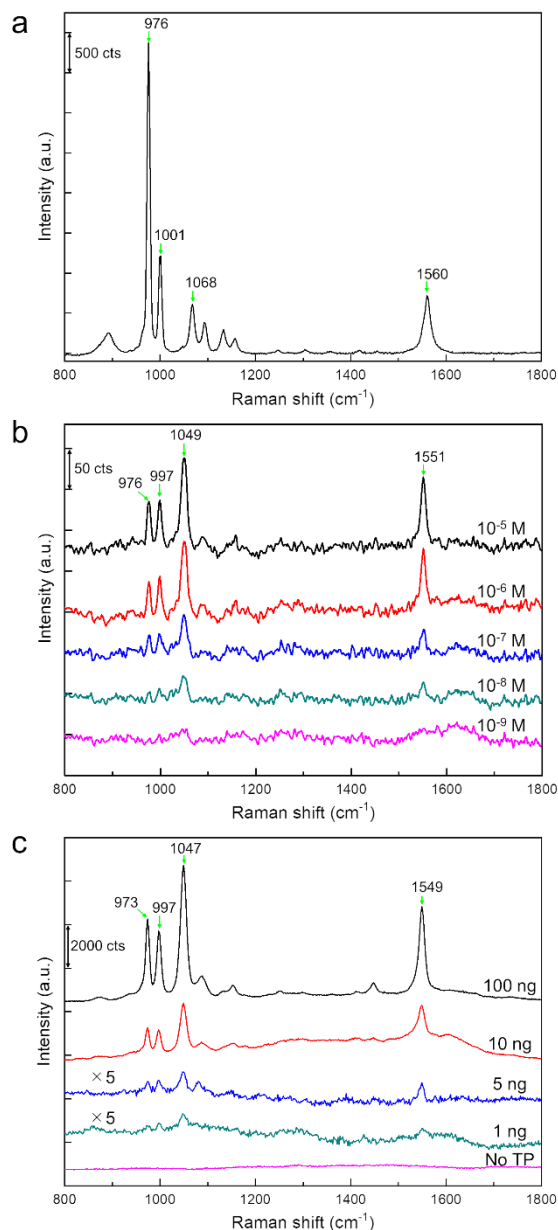


**Figure 8.** (a) Raman spectrum of neat TP. SERS spectra of trace amounts of TP (b) in aqueous solution with P-SiO<sub>2</sub>@Au NPs, and (c) on the P-FP substrate. P-SiO<sub>2</sub>@Au



NPs presented here were obtained with the standard synthetic condition. The spectra were off-set for clarity.

$N_{\text{Raman}}$  can be replaced with the concentration of the samples, giving

$$\text{EF} = \frac{I_{\text{SERS}}}{C_{\text{SERS}}} \times \frac{C_{\text{Raman}}}{I_{\text{Raman}}}$$

From the above calculation the EF of P-SiO<sub>2</sub>@Au NPs is experimentally determined to be  $4.3 \times 10^7$ – $8.5 \times 10^7$  (calculation details in Supporting Information), which is high among many reported noble metal-related SERS substrates.<sup>62–64</sup> The SERS effect can be attributed to electromagnetic (EM) and chemical enhancements. Though the clarification of chemical enhancement remains challenging, it is widely accepted that the enhanced local EM fields have major contributions to the total enhancement.<sup>65, 66</sup> The EM field distribution around P-SiO<sub>2</sub>@Au NP under 785 nm light irradiation is simulated with the FDTD method (Figure S8). There are localized EM fields of high intensity at the particle surface where the SNPs are embedded. The existence of SNP creates a metal-dielectric environment for EM enhancement,<sup>67</sup> leading to many “hot spots” for high SERS activity.

Paper-based SERS measurement allows simple, flexible, and low-cost trace detection on a practical basis.<sup>68</sup> The P-SiO<sub>2</sub>@Au NPs are employed in paper-based SERS measurements to test their potentials for practical applications. The paper-based SERS substrates are prepared through impregnating filter paper with the P-SiO<sub>2</sub>@Au NP suspension. The filter paper turns from white to bluish-purple after impregnation, indicating surface adsorption of the P-SiO<sub>2</sub>@Au NPs (Figure S9a and S9b, insets). SEM observation confirms the presence of P-SiO<sub>2</sub>@Au NPs on the fibrous structure of the filter paper (Figure S9b). Figure 8c shows the SERS spectra of trace amounts of TP detected with the P-SiO<sub>2</sub>@Au NP-loaded filter paper (P-FP) as the substrates. The mass detection limit by P-FP is *ca.* 1 ng of TP. For comparison, paper substrates loaded with spherical Au NPs (Au-FP) are also prepared (Figure S9c, S9d). The spherical Au NP is selected because it is one of the mainstream SERS-active materials in commercial paper-based SERS substrates. The mass detection limit by Au-FP is *ca.* 100 ng of TP (Figure S9e), which is two orders of magnitude greater than that of P-FP. The P-SiO<sub>2</sub>@Au NP is advantageous with great potential for practical uses.

## CONCLUSION

P-SiO<sub>2</sub>@Au NPs are prepared *via* one-step synthesis using arginine for Au reduction and SiO<sub>2</sub> formation at the same time. The products show tunable plasmon resonance within 580–730 nm depending on the amount of HAuCl<sub>4</sub> used for synthesis. TEM and DLS analysis show that HAuCl<sub>4</sub> addition increases the particle size at first ( $4.9$ – $36.4$   $\mu$ mol) and then causes a change in particle shape at a high dose ( $48.6$   $\mu$ mol). The particle size and shape changes are considered to cause the plasmon peak to red-shift with the

HAuCl<sub>4</sub> addition. FDTD simulations reveal the optical contribution from P-SiO<sub>2</sub>@Au NPs of different sizes and point to a possible new way of tuning the plasmon property with the SNPs. TEOS is important as the source to SNPs indispensable for the formation of pomegranate-like structure, while it can be replaced with preformed SNP sol. Arginine serves multiple roles, including reductant and capping agents for Au and catalyst for SiO<sub>2</sub>; it is also found to promote the combination of Au and SiO<sub>2</sub> probably through inducing electrostatic interactions. The P-SiO<sub>2</sub>@Au NPs achieve  $4.3 \times 10^7$ – $8.5 \times 10^7$  enhancement factor for colloidal SERS and *ca.* 1 ng mass detection limit for paper-based SERS measurements using thiophenol as the model analyte. They provide a promising candidate for advanced sensing and biomedical applications.

## ASSOCIATED CONTENT

**Supporting Information.** Supporting information is available free of charge via the Internet at <http://pubs.acs.org>. TEM analysis; XRD spectrum; models for FDTD simulation; time-course UV-Vis spectra and photographs; time-course pH measurements; SERS spectra using P-SiO<sub>2</sub>@Au NPs synthesized with different conditions; calculation details of EF; simulation results of EM field distribution; SEM analysis of blank filter paper and P-FP; SERS spectra using Au-FP substrates.

## AUTHOR INFORMATION

### Corresponding Author

\* E-mail: [shujunzh@hiroshima-u.ac.jp](mailto:shujunzh@hiroshima-u.ac.jp) (Shujun Zhou).

### Notes

The authors declare no completing financial interest.

## ACKNOWLEDGMENT

S. Zhou acknowledges the financial support from Grant-in-aid for Exploratory Research (2018) by Hiroshima University, and thanks Prof. Yoshinori Isomoto for providing the Raman spectrometer and Dr. Liang Yu for conducting the XRD measurements.

## REFERENCES

- (1) Li, J.-F.; Zhang, Y.-J.; Ding, S.-Y.; Panneerselvam, R.; Tian, Z.-Q. Core-Shell Nanoparticle-Enhanced Raman Spectroscopy. *Chem. Rev.* **2017**, *117*, 5002–5069.
- (2) Tang, Z.; Li, G.; Noble metal nanoparticle@metal oxide core/yolk-shell nanostructures as catalysts: recent progress and perspective. *Nanoscale* **2014**, *6*, 3995–4011.
- (3) Wang, H.; Chen, L.; Feng, Y.; Chen, H. Exploiting Core-Shell Synergy for Nanosynthesis and Mechanistic Investigation. *Acc. Chem. Res.* **2013**, *46*, 1636–1646.
- (4) Corma, A.; Garcia, H. Supported gold nanoparticles as catalysts for organic reactions. *Chem. Soc. Rev.* **2008**, *37*, 2096–2126.
- (5) Shao, L.; Zhuo, X.; Wang, J. Advanced Plasmonic Materials for Dynamic Color Display. *Adv. Mater.* **2017**, *1704338*.
- (6) Saha, K.; Agasti, S. S.; Kim, C.; Li, X.; Rotello, V. M. Gold Nanoparticles in Chemical and Biological Sensing. *Chem. Rev.* **2012**, *112*, 2739–2779.
- (7) Dreaden, E. C.; Alkilany, A. M.; Huang, X.; Murphy, C. J.; El-Sayed, M. A. The golden age: gold nanoparticles for biomedicine. *Chem. Soc. Rev.* **2012**, *41*, 2740–2779.

- (8) Guo, C. F.; Sun, T.; Cao, F.; Liu, Q.; Ren, Z. Metallic nanostructures for light trapping in energy-harvesting devices. *Light Sci. Appl.* **2014**, *3*, e161.
- (9) Daniel, M.-C.; Astruc, D. Gold nanoparticles: Assembly, Supramolecular Chemistry, Quantum-Size-Related Properties, and Applications toward Biology, Catalysis, and Nanotechnology. *Chem. Rev.* **2004**, *104*, 293–346.
- (10) Hanske, C.; Sanz-Qrtiz, M. N.; Liz-Marzán, L. M. Silica-Coated Plasmonic Metal Nanoparticles in Action. *Adv. Mater.* **2018**, *30*, 1707003.
- (11) Moreira, A. F.; Rodrigues, C. F.; Reis, C. A.; Costa, E. C.; Correia, I. J. Gold-core silica shell nanoparticles application in imaging and therapy: A review. *Micro. Meso. Mater.* **2018**, *270*, 168–179.
- (12) Liu, S.; Han, M.-Y. Silica-Coated Metal Nanoparticles. *Chem. Asian J.* **2010**, *5*, 36–45.
- (13) Liz-Marzán, L. M.; Giersig, M.; Mulvaney, P. Synthesis of Nanosized Gold-Silica Core-Shell Particles. *Langmuir* **1996**, *12*, 4329–4335.
- (14) Sánchez-Iglesias, A.; Claes, N.; Solís, D. M.; Taboada, J. M.; Bals, S.; Liz-Marzán, L. M.; Grzelczak, M. Reversible Clustering of Gold Nanoparticles under Confinement. *Angew. Chem. Int. Ed.* **2018**, *57*, 3183–3186.
- (15) Chen, P.-J.; Hu, S.-H.; Fan, C.-T.; Li, M.-L.; Chen, Y.-Y.; Chen, S.-Y.; Liu, D.-M. A novel multifunctional nano-platform with enhanced anti-cancer and photoacoustic imaging modalities using gold-nanorod-filled silica nanobeads. *Chem. Commun.* **2013**, *49*, 892–894.
- (16) Radloff, C.; Halas, N. J. Plasmonic Properties of Concentric Nanoshells. *Nano Lett.* **2004**, *4*, 1323–1327.
- (17) Pastoriza-Santos, I.; Gomez, D.; Pérez-Juste, J.; Liz-Marzán, L. M.; Mulvaney, P. Optical properties of metal nanoparticles coated silica spheres: a simple effective medium approach. *Phys. Chem. Chem. Phys.* **2004**, *6*, 5056–5060.
- (18) Graf, C.; van Blaaderen, A. Metalodielectric Colloidal Core-Shell Particles for Photonic Applications. *Langmuir* **2002**, *18*, 524–534.
- (19) Landon, P. B.; Mo, A. H.; Zhang, C.; Emerson, C. D.; Printz, A. D.; Gomez, A. F.; DeLaTorre, C. J.; Colburn, D. A. M.; Anzenberg, P.; Eliceiri, M.; O'Connell, C.; Lal, R. Designing Hollow Nano Gold Golf Balls. *ACS Appl. Mater. Interfaces* **2014**, *6*, 9937–9941.
- (20) Sebastian, V.; Lee, S.-K.; Jensen, K. F. Engineering the synthesis of silica-gold nano-urchin particles using continuous synthesis. *Nanoscale* **2014**, *6*, 13228–13235.
- (21) Rodríguez-Fernández, D.; Langer, J.; Henriksen-Lacey, M.; Liz-Marzán, L. M. Hybrid Au-SiO<sub>2</sub> Core-Satellite Colloids as Switchable SERS Tags. *Chem. Mater.* **2015**, *27*, 2540–2545.
- (22) Sanz-Ortiz, M. N.; Sentosun, K.; Bals, S.; Liz-Marzán, L. M. Templated Growth of Surface Enhanced Raman Scattering-Active Branched Gold Nanoparticles within Radial Mesoporous Silica Shells. *ACS Nano* **2015**, *9*, 10489–10497.
- (23) Wang, F.; Cheng, S.; Bao, Z.; Wang, J. Anisotropic Overgrowth of Metal Heterostructures Induced by a Site-Selective Silica Coating. *Angew. Chem. Int. Ed.* **2013**, *52*, 10344–10348.
- (24) Rodríguez-Fernández, D.; Altantzis, T.; Heidari, H.; Bals, S.; Liz-Marzán, L. M. A protecting group approach toward synthesis of Au-silica Janus nanostars. *Chem. Commun.* **2014**, *50*, 79–81.
- (25) Farrokhtakin, E.; Rodríguez-Fernández, D.; Mattoli, V.; Solís, D. M.; Taboada, J. M.; Obelleiro, F.; Grzelczak, M.; Liz-Marzán, L. M. Radial growth of plasmon coupled gold nanowires on colloidal templates. *J. Colloid Interface Sci.* **2015**, *449*, 87–91.
- (26) Chomette, C.; Duguet, E.; Mornet, S.; Yammine, E.; Manoharan, V. N.; Schade, N. B.; Hubert, C.; Ravaine, S.; Perro, A.; Treguer-Delapierre, M. Templated growth of gold satellites on dimpled silica cores. *Faraday Discuss.* **2016**, *191*, 105–116.
- (27) Mühlig, S.; Cunningham, A.; Scheeler, S.; Pacholski, C.; Bürgi, T.; Rockstuhl, C.; Lederer, F. Self-Assembled Plasmonic Core-Shell Clusters with an Isotropic Magnetic Dipole Response in the Visible Range. *ACS Nano* **2011**, *5*, 6586–6592.
- (28) Le Beulze, A.; Gomez-Graña, S.; Gehan, H.; Mornet, S.; Ravaine, S.; Correa-Duarte, M.; Guerrini, L.; Alvarez-Puebla, R. A.; Duguet, E.; Pertreux, E.; Crut, A.; Maioli, P.; Vallée, F.; Del Fatti, N.; Ersen, O.; Treguer-Delapierre, M. Robust raspberry-like metallo-dielectric nanoclusters of critical sizes as SERS substrates. *Nanoscale* **2017**, *9*, 5725–5736.
- (29) Liz-Marzán, L. M.; Giersig, M.; Mulvaney, P. Homogeneous silica coating of vitreophobic colloids. *Chem. Commun.* **1996**, 731–732.
- (30) Jones, M. R.; Osberg, K. D.; Macfarlane, R. J.; Langille, M. R.; Mirkin, C. A. Templated Techniques for the Synthesis and Assembly of Plasmonic Nanostructures. *Chem. Rev.* **2011**, *111*, 3736–3827.
- (31) Walsh, T. R.; Knecht, M. R. Biointerface Structural Effects on the Properties and Applications of Bioinspired Peptide-Based Nanomaterials. *Chem. Rev.* **2017**, *117*, 12641–12704.
- (32) Slocik, J. M.; Wright, D. W. Biomimetic Mineralization of Noble Metal Nanoclusters. *Biomolecules* **2003**, *4*, 1135–1141.
- (33) Hu, B.; Wang, S.-B.; Wang, K.; Zhang, M.; Yu, S.-H. Microwave-Assisted Rapid Facile “Green” Synthesis of Uniform Silver Nanoparticles: Self-Assembly into Multilayered Films and Their Optical Properties. *J. Phys. Chem. C* **2008**, *112*, 1169–1174.
- (34) Plascencia-Villa, G.; Torrente, D.; Marucho, M.; José-Yacamán, M. Biodirected Synthesis and Nanostructural Characterization of Anisotropic Gold Nanoparticles. *Langmuir* **2015**, *31*, 3527–3536.
- (35) Sebastián, V.; Lee, S.-K.; Zhou, C.; Kraus, M. F.; Fujimoto, J. G.; Jensen, K. F. One-step continuous synthesis of biocompatible gold nanorods for optical coherence topography. *Chem. Commun.* **2012**, *48*, 6654–6656.
- (36) Fu, G.-T.; Liu, C.; Wu, R.; Chen, Y.; Zhu, X.-S.; Sun, D.-M.; Tang, Y.-W.; Lu, T.-H. L-Lysine mediated synthesis of platinum nanocuboids and their electrocatalytic activity towards ammonia oxidation. *J. Mater. Chem. A* **2014**, *2*, 17883–17888.
- (37) Fu, G.-T.; Jiang, X.; Wu, R.; Wei, S.-H.; Sun, D.-M.; Tang, Y.-W.; Lu, T.-H.; Chen, Y. Arginine-Assisted Synthesis and Catalytic Properties of Single-Crystalline Palladium Tetrapods. *ACS Appl. Mater. Interfaces* **2014**, *6*, 22790–22795.
- (38) Lee, H.-E.; Ahn, H.-Y.; Mun, M.; Lee, Y. Y.; Kim, M.; Cho, N. H.; Chang, K.; Kim, W. S.; Rho, J.; Nam, K. T. Amino-acid- and peptide-directed synthesis of chiral plasmonic gold nanoparticles. *Nature* **2018**, *556*, 360–365.
- (39) Ozaki, M.; Sakashita, S.; Hamada, Y.; Usui, K. Peptides for Silica Precipitation: Amino Acid Sequences for Directing Mineralization. *Protein Peptide Lett.* **2018**, *25*, 15–24.
- (40) Yokoi, T.; Sakamoto, Y.; Terasaki, O.; Kubota, Y.; Okubo, T.; Tatsumi, T. Periodic Arrangement of Silica Nanospheres Assisted by Amino Acids. *J. Am. Chem. Soc.* **2006**, *128*, 13664–13665.
- (41) Hartlen, K. D.; Athanasopoulos, A. P. T.; Kitaev, V. Facile Preparation of Highly Monodisperse Small Silica Spheres (15 to > 200 nm) Suitable for Colloidal Templating and Formation of Ordered Arrays. *Langmuir* **2008**, *24*, 1714–1720.
- (42) Davis, T. M.; Snyder, M. A.; Krohn, J. E.; Tsapatsis, M. Nanoparticles in Lysine-Silica Sols. *Chem. Mater.* **2006**, *18*, 5814–5816.
- (43) Frens, G. Controlled Nucleation for the Regulation of the Particle Size on Monodisperse Gold Suspensions. *Nat. Phys. Sci.* **1973**, *241*, 20–22.
- (44) Johnson, P. B.; Christy, R. W. *Phys. Rev. B* **1972**, *6*, 4370–4379.
- (45) Palik, E. D. *Handbook of Optical Constants of Solids*; Academic Press; San Diego; 1998.

- (46) Dong, Y.; Hajfathalian, M.; Maidment, P. S. N.; Hsu, J. C.; Naha, P. C.; Si-Mohamed, S.; Beruilly, M.; Kim, J.; Chhour, P.; Douek, P.; Litt, H. I.; Cormode, D. P. Effect of Gold Nanoparticle Size on Their Properties as Contrast Agents for Computed Tomography. *Sci. Rep.* **2019**, *9*, 14912.
- (47) Ghosh, S. K.; Pal, T. Interparticle Coupling Effect on the Surface Plasmon Resonance of Gold Nanoparticles: From Theory to Applications. *Chem. Rev.* **2007**, *107*, 4797–4862.
- (48) Li, Y.-F.; Lv, J.-J.; Wang, A.-J.; Zhang, M.; Wang, R.-Z.; Feng, J.-J. L-Arginine-assisted electrochemical fabrication of hierarchical gold dendrites with improved electrocatalytic activity. *J. Solid State Electrochem.* **2015**, *19*, 3185–3193.
- (49) Fitch, C. A.; Platzer, G.; Okon, M.; Garcia-Moreno E., B.; McIntosh, L. P. Arginine: its pKa value revisited. *Protein Sci.* **2015**, *24*, 752–761.
- (50) Wright, L. B.; Merrill, N. A.; Knecht, M. R.; Walsh, T. R. Structure of Arginine Overlayers at the Aqueous Gold Interface: Implications for Nanoparticle Assembly. *ACS Appl. Mater. Interfaces* **2014**, *6*, 10524–10533.
- (51) Iler, R. K. *The Chemistry of Silica*; Wiley: New York, 1979.
- (52) Witten, T. A.; Sander, L. M. Diffusion-limited aggregation. *Phys. Rev. B* **1983**, *27*, 5686–5697.
- (53) KulKarni, A. A.; Cabeza, V. S. Insights in the Diffusion Controlled Interfacial Flow Synthesis of Au Nanostructures in a Microfluidic System. *Langmuir* **2017**, *33*, 14315–14324.
- (54) Lin, G.; Lu, W.; Cui, W.; Jiang, L. A Simple Synthesis Method for Gold Nano- and microplate Fabrication Using a Tree-Type Multiple-Amine Head Surfactant. *Cryst. Growth Design* **2010**, *10*, 1118–1123.
- (55) Yan, F.; Liu, L.; Walsh, T. R.; Gong, Y.; El-Khoury, P. Z.; Zhang, Y.; Zhu, Z.; De Yoreo, J. J.; Engelhard, M. H.; Zhang, X.; Chen, C.-L. Controlled synthesis of highly-branched plasmonic gold nanoparticles through peptoid engineering. *Nat. Commun.* **2018**, *9*, 2327.
- (56) Wang, J.; Sugawara-Narutaki, A.; Fukao, M.; Yokoi, T.; Shimojima, A.; Okubo, T. Two-Phase Synthesis of Monodisperse Silica Nanospheres with Amines or Ammonia Catalyst and Their Controlled Self-Assembly. *ACS Appl. Mater. Interfaces* **2011**, *3*, 1538–1544.
- (57) Aggarwal, R. L.; Farrar, L. W.; Greeneltch, N. G.; Van Duyne, R. P.; Polla, D. L. Measurement of the Raman Line Widths of Neat Benzenethiol and a Self-Assembled Monolayer (SAM) of Benzenethiol on a Silver-Coated Surface-Enhanced Raman Scattering (SERS) Substrate. *Appl. Spectrosc.* **2012**, *66*, 740–743.
- (58) Saikin, S. K.; Chu, Y.; Rappoport, D.; Crozier, K. B.; Aspuru-Guzik, A. Separation of Electromagnetic and Chemical Contributions to Surface-Enhanced Raman Spectra on Nanoengineered Plasmonic Substrates. *J. Phys. Chem. Lett.* **2010**, *1*, 2740–2746.
- (59) Pannico, M.; Calarco, A.; Peluso, G.; Musto, P. Functionalized Gold Nanoparticles as Biosensors for Monitoring Cellular Uptake and Localization in Normal and Tumor Prostatic Cells. *Biosensors* **2018**, *8*, 87.
- (60) Holze, R. The adsorption of thiophenol on gold – a spectroelectrochemical study. *Phys. Chem. Chem. Phys.* **2015**, *17*, 21364–21372.
- (61) Kim, C.; Baek, S.; Ryu, Y.; Kim, Y.; Shin, D.; Lee, C.-W.; Park, W.; Urbas, A. M.; Kang, G.; Kim, K. Large-scale nanoporous metal-coated silica aerogels for high SERS effect improvement. *Sci. Rep.* **2018**, *8*, 15144.
- (62) Liu, K.; Bai, Y.; Zhang, L.; Yang, Z.; Fan, Q.; Zheng, H.; Yin, Y.; Gao, C. Porous Au-Ag Nanospheres with High-Density and Highly Accessible Hotspots for SERS Analysis. *Nano. Lett.* **2016**, *16*, 3675–3681.
- (63) Demirel, G.; Usta, H.; Yilmaz, M.; Celik, M.; Alidagi, H. A.; Buyukserin, F. Surface-enhanced Raman spectroscopy (SERS): an adventure from plasmonic metals to organic semiconductors as SERS platforms. *J. Mater. Chem. C* **2018**, *6*, 5314–5335.
- (64) Liu, H.; Yang, L.; Liu, J. Three-dimensional SERS hot spots for chemical sensing: Towards developing a practical analyzer. *Trend Ana. Chem.* **2016**, *80*, 364–372.
- (65) Kneipp, K. Chemical Contributions to SERS Enhancement: An Experimental Study on a Series of Polymethine Dyes on Silver Nanoaggregates. *J. Phys. Chem. C* **2016**, *120*, 21076–21081.
- (66) Zeng, Z.; Liu, Y.; Wei, J. Recent advances in surface-enhanced Raman spectroscopy (SERS): Finite-difference time-domain (FDTD) method for SERS and sensing applications. *Trend Ana. Chem.* **2016**, *75*, 162–173.
- (67) Kodali, A. K.; Llorca, X.; Bhargava, R. Optically designed nanolayered metal-dielectric particles as probes for massively multiplexed and ultrasensitive molecular assays. *PNAS* **2010**, *107*, 13620–13625.
- (68) Lee, C. H.; Tian, L.; Singamaneni, S. Paper-Based SERS Swab for Rapid Trace Detection on Real-World Surface. *ACS Appl. Mater. Interfaces* **2010**, *2*, 3429–3435.



## Table of Contents

